Dyes and Pigments 146 (2017) 374–385

Contents lists available at ScienceDirect

Dyes and Pigments

journal homepage: www.elsevier.com/locate/dyepig

# Effect of intermolecular interaction with phenothiazine core on inverted organic photovoltaics by using different acceptor moiety

Yu-Lung Weng [a, 1], Yi-Chan Li [b, 1], Chih-Ping Chen [b, *], Yuan Jay Chang [a, **]

[a] Department of Chemistry, Tunghai University, NO. 1727, Sec.4, Taiwan Boulevard, Xitun District, Taichung 40704, Taiwan
[b] Department of Materials Engineering, Ming Chi University of Technology, 84 Gungjuan Rd., Taishan Dist, New Taipei City 24301, Taiwan

ARTICLE INFO

*Article history:*
Received 23 May 2017
Received in revised form
16 June 2017
Accepted 14 July 2017
Available online 15 July 2017

*Keywords:*
Inverted organic photovoltaics (OPVs)
Solution-processed bulk heterojunction (BHJ)
Small-molecule organic photovoltaics (SMOPVs)
A–D–A
A–D–D–A

ABSTRACT

Six novel small molecules containing phenothiazine as the core moiety of p-type materials were synthesized in combination with $PC_{61}BM$ or $PC_{71}BM$ as n-type materials for bulk heterojunction organic photovoltaic (OPV) cells. Phenothiazine was used as donor building blocks to construct acceptor–donor–acceptor (A–D–A) and A–D–D–A small molecule. We investigated the relationship between the molecular structures, optoelectronic and thermal properties, and their blend film morphologies for OPV applications. We further studied their photophysical properties using a time-dependent density functional theory model and the B3LYP functional. A solution-processed OPV employing **PT2-DE** combined with the electron acceptor $PC_{61}BM$ and additive DIO achieved optimal device performance, with a short-circuit current of 6.3 mA $cm^{-2}$, an open-circuit voltage of 770 mV, a fill factor of 0.55, and a corresponding overall conversion efficiency of 2.64%. To the best of our knowledge, this is the best-reported performance of a phenothiazine derivative for OPV application.



## 1. Introduction

In recent years, because of the depletion of fossil fuels and increased greenhouse gas emissions that have resulted in the problem of global warming, the investigation and development of alternative renewable and environmentally friendly energy sources has become increasingly important. In particular, solar energy has been acknowledged as a potential alternative energy resource. Organic photovoltaics (OPVs) convert sunlight directly into electricity. OPV solar cells have attracted considerable attention because of their portability, easy fabrication, energy level tunable by functional groups in the molecular structure, compatibility with flexible substrates, and low-cost roll-to-roll processing [1–3].

A general preconception regarding OPVs is that the use of a conjugated polymer as a p-type material and fullerene derivatives as a n-type material can achieve high power conversion efficiency (PCE). With the advancement of device engineering and molecular design, polymer-based solar cells have been demonstrated in excess of 12% by using a solution-processed bulk heterojunction (BHJ) [4–6]. Polymeric materials can be roughly classified into two broad types: homopolymer and donor–acceptor copolymers. Donor–acceptor copolymers exhibit a wide absorption region and favorable film morphologies, resulting in high device performance [7,8]. A comparison of polymeric materials reveals that small molecules (SMs) possess predominant advantages such as well-defined molecular structures and higher reliability, higher reproducibility, and easier energy level tuning and device fabrication than large molecules. The use of solution processing for device fabrication is generally considered to enable large production through inject printing or roll-to-roll coating, which are more cost-effective than vacuum deposition. Therefore, several studies have investigated small-molecule OPVs (SMOPVs), which have PCEs of more than 10%, by using solution-processed fabrication techniques [9–11]. The high device performance achieved using SMOPVs suggests a new direction for innovative ideas regarding the design of novel SMs with tailor-made structures and designated physical characteristics. Novel small-molecule-based p-type materials in OPVs have been used to develop a wide variety of promising organic materials with different donor–acceptor moiety combinations such as symmetrical acceptor–donor–acceptor (A–D–A) [12–14] and

* Corresponding author.
** Corresponding author.
*E-mail addresses:* cpchen@mail.mcut.edu.tw (C.-P. Chen), jaychang@thu.edu.tw (Y.J. Chang).
[1] These authors contributed equally to this work.

http://dx.doi.org/10.1016/j.dyepig.2017.07.027
0143-7208/

donor–acceptor–donor (D–A–D) [15–17] combinations. Systems with PCEs similar to those of polymeric systems have been developed [9]. A variety of photovoltaic materials with prominent chemical frameworks that were produced using solution-processed deposition have been reported; these include oligothiophene [18,19], fused polycycle [20–22], diketopyrrollopyrrole [23,24], phathalocyanine [25,26], and isoindigo [27,28].

Weak intermolecular interactions between SMs of p-type materials can hamper charge transport, resulting in a low fill factor (FF) [29]. Intermolecular interaction is a key factor that determines the stacking structures of a p-type material; thus, it significantly affects electrical properties and device performance, and it can result in the enhancement of FF and PCE. Extending π-stacking moieties and increasing coplanarity enhances the intermolecular interactions between p-type materials. Although several studies have investigated the influence of π–π stacking interactions between SMs of p-type material on the performance of OPVs, few studies have focused on other intermolecular interactions such as hydrogen bonding or dipole–dipole interaction [17,30].

Phenothiazine has been shown to be a good electron-donating moiety, and it is used in organic light-emitting diodes [31] and dye-sensitized solar cells [32–34]. However, few studies have successfully demonstrated the use of phenothiazine as a building block for OPVs [34,35]. Maglione et al. used phenothiazine as donor blocks and constructed a D–A–D material for OPV application that had a PCE of 0.7%, the highest reported for phenothiazine derivatives [36]. In the present study, we used phenothiazine as an electron-donating moiety, coupled with three acceptors applied to A–D–A and A–D–D–A dipolar systems as p-type materials. We fabricated an inverted OPV device with indium tin oxide (ITO)/ZnO/active layers/$MoO_3$/Ag using solution-processed deposition; the OPV device employing material **PT2-DE** combined with electron acceptor $PC_{61}BM$ and 1,8-diiodooctane (DIO) achieved a high PCE of 2.64%. To the best of our knowledge, this is the highest ever PCE reported for phenothiazine-based SMs for OPV application. The high PCE can be attributed to the high $V_{oc}$ of 0.77 V.

## 2. Results and discussion

### 2.1. Synthesis of A–D–A and A–D–D–A molecules

The structures of phenothiazine-based SMs and their synthetic sequences are presented in Fig. 1 and Scheme 1. Molecule **1** was synthesized first; one or two bromo substituents were subsequently added through a bromination reaction to yield **2** or **4**. The number of core structure units was increased by adding another phenothiazine moiety through a Stille coupling reaction; thereafter, bromination reaction was performed to yield **6**. A thiophene unit, used to extend π-conjugation, was connected to **2** and **6** through a Stille coupling reaction to yield **3** and **7** [37]. The six p-type materials were obtained through Knoevenagel condensation to build three types of acceptor unit by using malononitrile, ethyl 2-cyanoacetate, and 2-cyano-*n*-hexylacetamide [38]. All the new compound structures were characterized using spectroscopy.

### 2.2. Thermal stability

Favorable thermal stability is essential for p-type organic materials because photovoltaic devices are operated under sunlight in a relatively high-temperature environment. The thermal properties of the **PT**-series were investigated using thermal gravimetric analysis (Fig. 2 and Table 1). The thermal stability of the SMs decreased in the order **PT2**-series > **PT1**-series for the core moiety and **DCN** > **DAM** > **DE** for the acceptor unit. The decomposition temperature $T_d$ (corresponding to 5% weight loss) of these compounds, which was greater than 350 °C, indicated the good thermal stability of these phenothiazine-based SMs. **PT1-DCN** and **PT2-DCN** exhibited relatively superior thermal stability with decomposition temperatures of 395 and 404 °C under $N_2$ conditions.

### 2.3. Optoelectronic properties of the molecules

The optical absorption spectra of all **PT**-series materials in methylene chloride solution and those of their thin films are presented in Fig. 3 and S13, and their photochemical and electrochemical parameters are listed in Table 1. The spectra of all p-type materials exhibit two broad and high-intensity absorption peaks in the range 360–563 nm. Similar absorption was discovered for the materials in solution as for those in film form; the short-wavelength region of 360–391 nm is attributed to localized π-π* and n-π* transitions, whereas the long-wavelength region of 486–563 nm is due to intramolecular charge-transfer (ICT) transitions. The ICT transitions decreased in the order **PT1**-series > **PT2**-series for the core moiety and **DCN** > **DE** > **DAM** for the acceptor unit. We assumed that the dicyanovinylene group possesses a stronger electron-withdrawing ability than the ester and amide moieties. The solid state of ICT transition in thin film form showed a bathochromatic shift of approximately 6–31 nm with respect to that in DCM solution, which indicated intermolecular J-aggregation on the surface of the substance. The spectra of the compounds **PT1-DCN** and **PT2-DCN** have a large absorption region and large full width at half maximum of the ICT band.

The ionic potentials (IPs) corresponding to the highest occupied molecular orbitals (HOMO) of the molecules were measured using cyclic voltammetry (Fig. 3, S18 and S19). The electron affinity levels of the molecules were estimated from the HOMO levels and

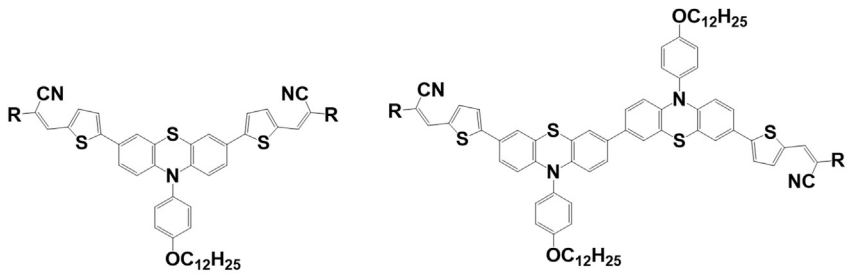


PT1-DCN R= CN
PT1-DE R= COOEt
PT1-DAM R= $CONHC_6H_{13}$

PT2-DCN R= CN
PT2-DE R= COOEt
PT2-DAM R= $CONHC_6H_{13}$

**Fig. 1.** The structures of **PT**-series for OPVs p-type materials.

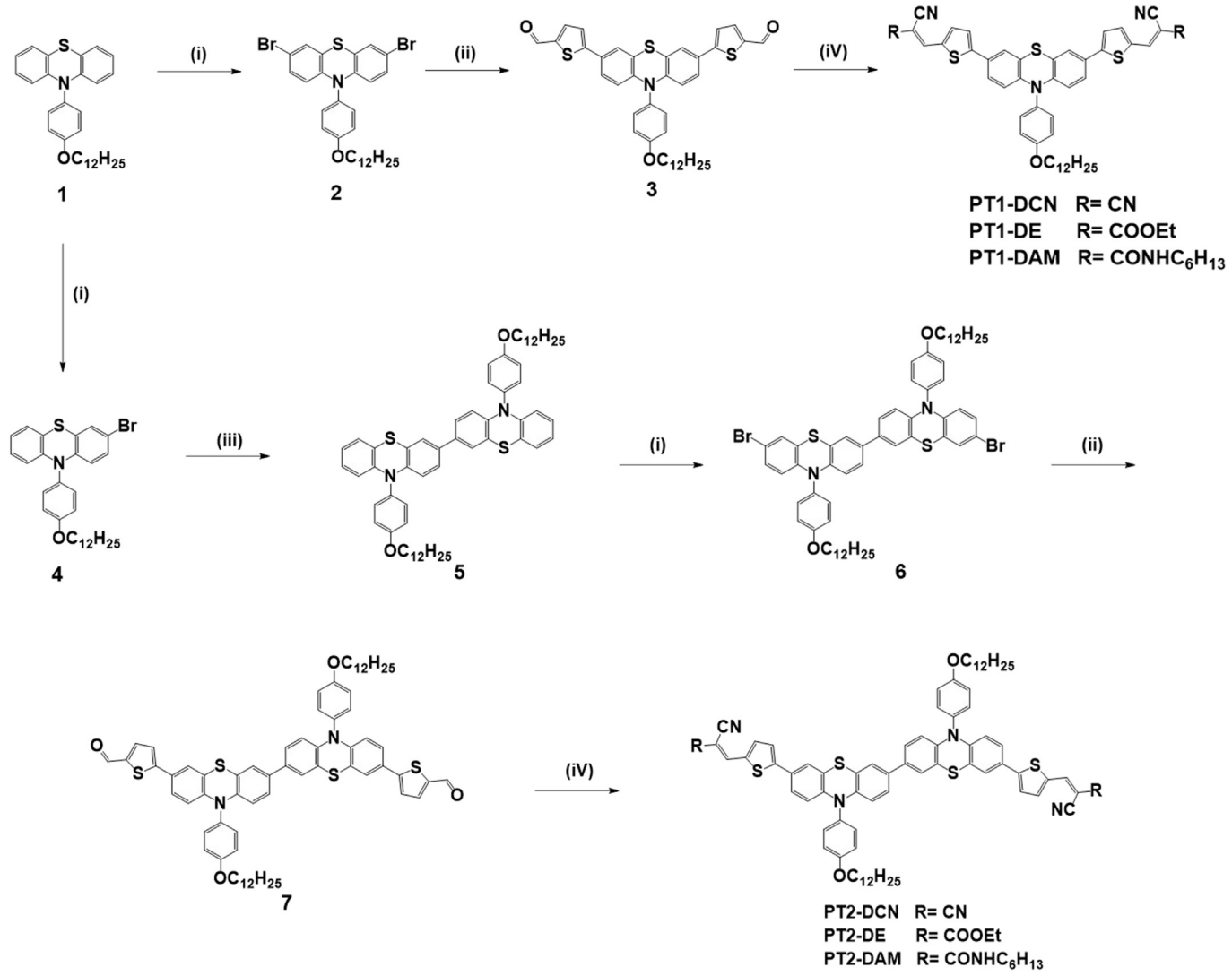


**Scheme 1.** Synthesis route of **PT**-series SM. i) NBS, $CH_2Cl_2$; ii) (5-(1,3-dioxolan-2-yl)thiophen-2-yl)tributyl-stannane, $PdCl_2(PPh_3)_2$, DMF, 110 °C; iii) a. n-BuLi/triisopropyl borate, −78 °C; followed by 3 M HCl.; b. $Pd(PPh_3)_4$, compound **4**, 2 M $K_2CO_3$, toluene/THF = 1.5/1.; iv) Malononitrile or Ethyl cyanoacetate or 2-Cyano-*N*-hexylacetamide, $CH_3COONH_4$, THF, reflux/Piperidine, Toluene, reflux.

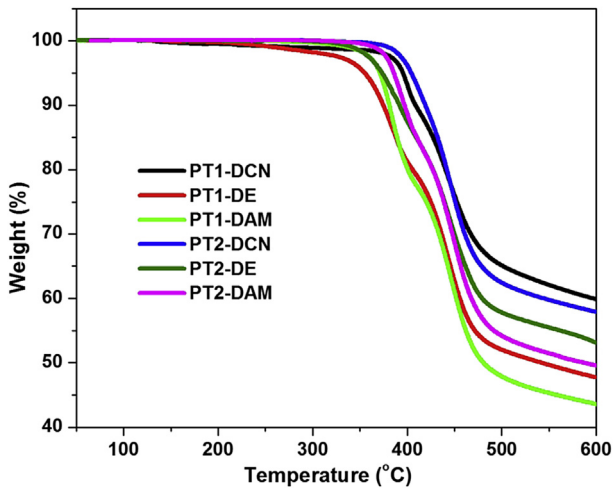


**Fig. 2.** Thermogravimetric analysis of **PT**-series with a heating rate 10 °C $min^{-1}$ under $N_2$.

zero–zero bandgaps at the onset of the absorption spectra (Table 1). Clearly, in the dipolar system of the **PT**-series p-type materials, the electron-withdrawing moiety strongly affects the IPs and electron delocalization. The structure skeleton contains the dicyanovinylene group because the electron-withdrawing groups of **PT1-DCN** and **PT2-DCN** were shown to have larger IP energy levels than the ethyl cyanoacrylate and cyano-*N*-hexylacrylamide groups. The compounds **PT1-DCN** and **PT2-DCN** also had a narrow HOMO–lowest unoccupied molecular orbital (LUMO) energy gap, which is consistent with the wide absorption ranges and more red-shifted ICT absorption bands illustrated in Fig. 3. For proper operation of an OPV containing it, the compound **PT1-DCN** had the deepest HOMO energy level and its small bandgap should give corresponding devices a high $V_{oc}$ and $J_{sc}$.

### 2.4. Computational analysis

The electronic characteristics of **PT**-series SMs were investigated using theoretical models. Full geometrical optimizations were performed using the B3LYP/6-31G* hybrid functional, which was implemented in Q-Chem 3.0 [39]. The optimized molecular

**Table 1**
Photochemical and electrochemical parameters of donor materials.

| P-type material | HOMO/LUMO[a] (eV) | Band gap[a] (eV) | $f^a$ | $\lambda_{max(sol)}$[b] | $\lambda_{max(film)}$ (nm) | $T_d$[c] (°C) | IP[d] (eV) | $E_g$[e] (eV) | EA[f] (eV) |
|---|---|---|---|---|---|---|---|---|---|
| **PT1-DCN** | −5.51/-3.02 | 2.49 | 0.8344 | 386, 537 | 379, 549 | 395 | −5.19 | 1.93 | −3.26 |
| **PT1-DE** | −5.24/-2.63 | 2.61 | 0.8797 | 378, 511 | 374, 521 | 355 | −5.15 | 2.00 | −3.15 |
| **PT1-DAM** | −5.15/-2.45 | 2.70 | 0.9192 | 372, 496 | 369, 502 | 371 | −5.13 | 2.08 | −3.05 |
| **PT2-DCN** | −5.13/-2.81 | 2.32 | 0.6098 | 380, 532 | 391, 563 | 404 | −5.04 | 1.91 | −3.13 |
| **PT2-DE** | −4.94/-2.47 | 2.47 | 0.6752 | 367, 502 | 375, 525 | 373 | −4.99 | 2.03 | −2.96 |
| **PT2-DAM** | −4.88/-2.29 | 2.59 | 0.6488 | 360, 486 | 366, 505 | 386 | −5.00 | 2.11 | −2.89 |

[a] TDDFT/B3LYP calculated values.
[b] Absorption in DCM and film.
[c] $T_d$ point obtained from TGA.
[d] Ionic potentials were measured using cyclic voltammetry.
[e] $E_g$ calculated by the onset of absorption spectra.
[f] EA calculated by IP − $E_g$.

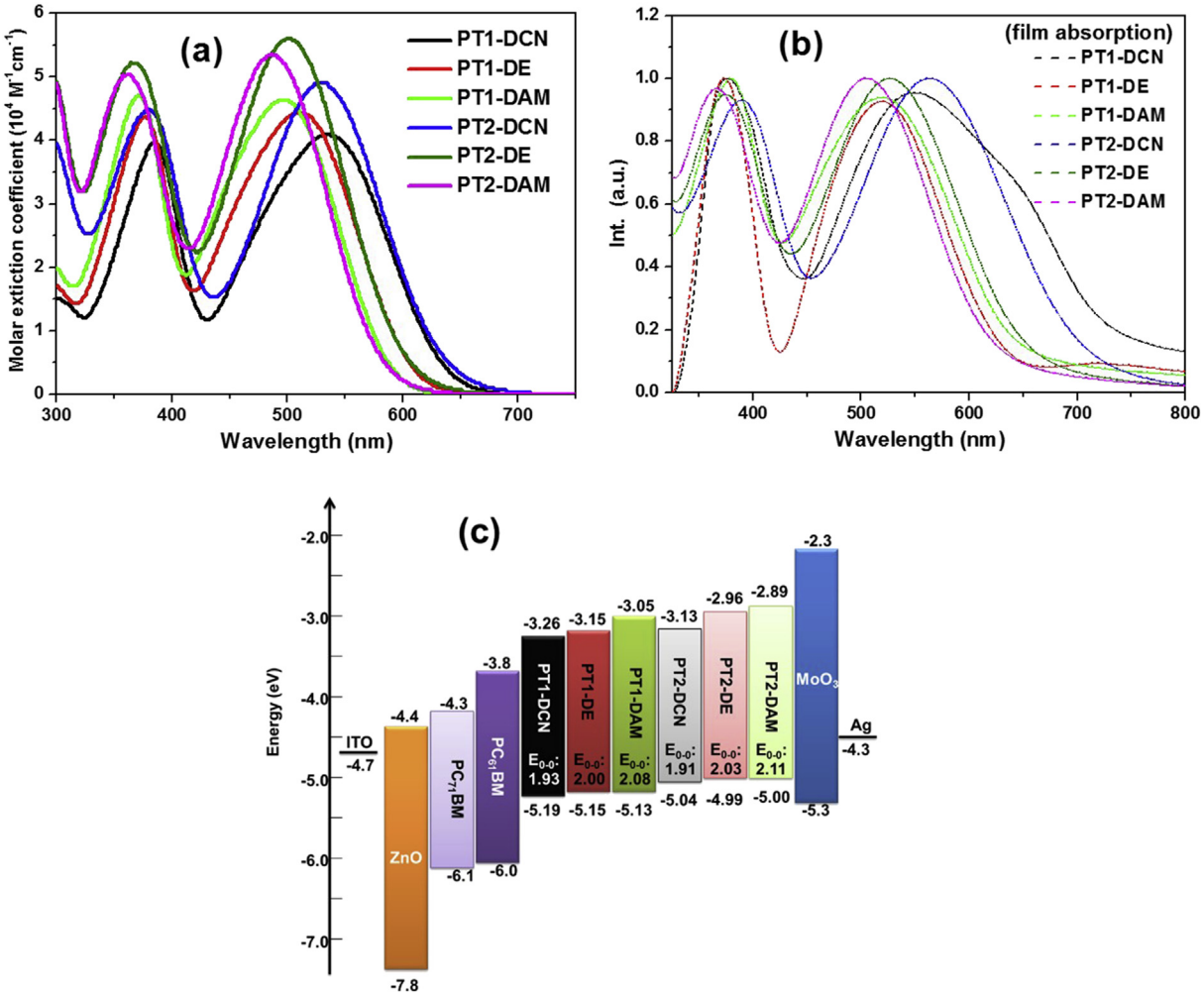


**Fig. 3.** Absorption spectra of molecules in (a) DCM solution; (b) thin films, and (c) energy diagrams of these p-type materials and other materials use in this study.

geometry of the **PT**-series SMs is shown in Fig. 4 and S17. Clearly, the phenothiazine core unit of the adjacent thiophene rings was slightly twisted; however, the orientation of the adjacent phenothiazine in the **PT2**-series was twisted by 36°–38° because of steric hindrance. This slight distortion in SM conformation did not inhibit electron transport between the electron donor and electron acceptor moieties. As depicted in Fig. 4 and S16, the electron densities of the HOMOs were mainly distributed around the phenothiazine donor sites, whereas those of the LUMOs were distributed around the acceptor moieties. Accordingly, HOMO to LUMO transitions contributed more than 92% to the first-singlet excited state (S1 state) and oscillator strength (*f*) beyond 0.6 in all **PT**-series materials.

The bar chart in Fig. 3c indicates that **PT1-DCN** had a higher HOMO energy level than the other compounds; the trends **PT1-DCN** > **PT1-DE** ≈ **PT1-DAM** and **PT2-DCN** > **PT2-DE** ≈ **PT2-DAM** are consistent with the computational results. The energy gap of the p-type materials could be verified from the dipole moment:

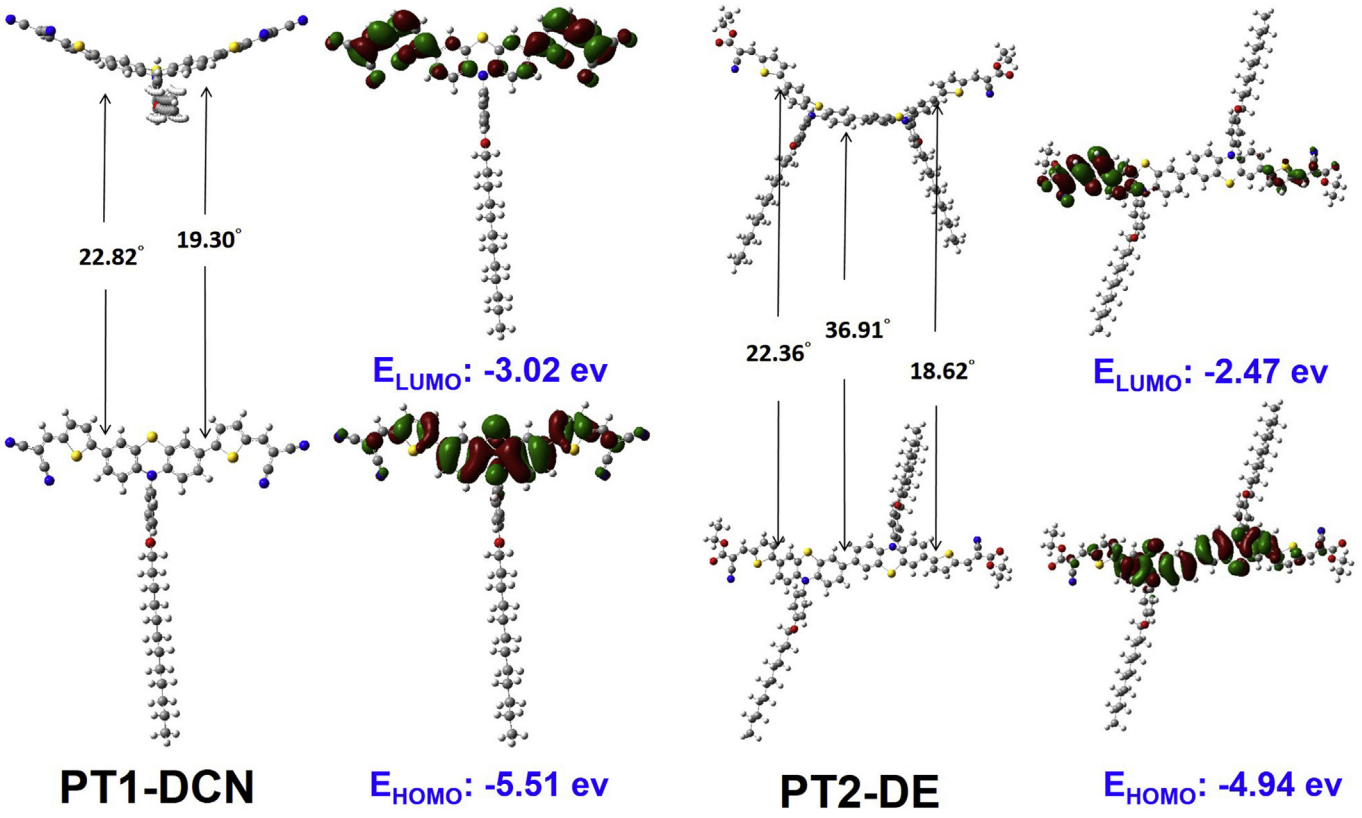


**Fig. 4.** Computed optimum structure and frontier molecular orbitals of **PT1-DCN** and **PT2-DE** calculated with TDDFT (B3LYP/6-31G*) in vacuum.

**PT1-DCN** (8.5314 D) and **PT2-DCN** (11.0752 D) had a larger dipole moment than the others (Table S1); the trends **PT1-DCN** > **PT1-DE** > **PT1-DAM** and **PT2-DCN** > **PT2-DE** > **PT2-DAM** are consistent with the absorption results both for the SMs in methlyene chloride and in film form. The large dipole moment of the molecules can be attributed to the strong electron-donating moiety of dicyanovinylene in **PT1-DCN** and **PT2-DCN**. The p-type material **PT1-DCN** had the deepest HOMO energy level (−5.51 eV) and the largest gap ($p\text{-type}_{HOMO}-n\text{-type}_{LUMO}$) to the LUMO energy level of the n-type materials $PC_{61}BM$ or $PC_{71}BM$; this result is consistent with the experiment data obtained through CV (−5.19 eV). We expected that the **PT1-DCN** would have a high $V_{oc}$ in a corresponding OPV device, and this was verified by fabricating devices using solution-processed deposition.

### 2.5. Photovoltaic performance of OPVs

We fabricated OPV devices with a layer structure of ITO [Sanyo, Japan (8 Ω $square^{-1}$)]/ZnO/active layers/$MoO_3$/Ag and an active area of 10 $mm^2$. The detailed fabrication conditions are provided in the supporting information (SI). The ZnO layer (40 nm thick) was prepared from a 0.5 M zinc acetate precursor solution in 2-methoxyethanol and deposited on top of the ITO [40,41]. The ZnO layer was annealed in air at 160 °C for 30 min prior to use. The active layer solution of **PT**-series SMs containing $PC_{61}BM$ or $PC_{71}BM$ (1:1.5) was stirred in $CHCl_3$ with or without DIO overnight, filtered through a polytetrafluoroethylene (0.2 μm) filter, and then spin-coated onto the ZnO layer. Incident photocurrent conversion efficiency (IPCE) and photocurrent–voltage (*J*–*V*) curves were measured for all molecules under AM 1.5 solar light (100 mW $cm^{-2}$); $J_{sc}$, $V_{oc}$, FF, and PCE are presented in Tables 2 and 3, and the *J*–*V* curves and IPCEs of the constructed OPV devices are shown in Figs. 5 and 6. The PCE of **PT1-DCN**/$PC_{61}BM$, **PT1-DE**/$PC_{61}BM$, and **PT1-DAM**/$PC_{61}BM$ was 0.85%, 0.52%, and 0.51%, respectively. The slightly higher PCE of the **PT1-DCN** device can be attributed to its higher $J_{sc}$, which is consistent with its lower energy

**Table 2**
Photovoltaic parameters of devices made **PT1**-series p-type materials with $PC_{61}BM$ and $PC_{71}BM$ as active layer.

| Active layer (weight ratio) | $V_{oc}$ (V) | $J_{sc}$ (mA·$cm^{-2}$) | FF (%) | PCE (%) | $R_S$ (Ω $cm^2$) | $R_{SH}$ (Ω $cm^2$) |
|---|---|---|---|---|---|---|
| **PT1-DCN**/$PC_{61}BM$[a] | 0.75 | 3.6 | 30.8 | 0.85 | 75 | 284 |
| **PT1-DCN**/$PC_{61}BM$[b] | 0.77 | 6.0 | 42.7 | 1.97 | 35 | 452 |
| **PT1-DCN**/$PC_{71}BM$[b] | 0.78 | 7.8 | 39.8 | 2.42 | 33 | 248 |
| **PT1-DE**/$PC_{61}BM$[a] | 0.72 | 2.2 | 32.5 | 0.52 | 167 | 434 |
| **PT1-DE**/$PC_{61}BM$[b] | 0.78 | 2.3 | 33.3 | 0.59 | 186 | 515 |
| **PT1-DAM**/$PC_{61}BM$[a] | 0.69 | 2.2 | 33.0 | 0.51 | 172 | 511 |
| **PT1-DAM**/$PC_{61}BM$[b] | 0.80 | 1.6 | 36.0 | 0.48 | 167 | 769 |

[a] p-type/n-type ratio of 1/1.5.
[b] With DIO additive (1.5%).

**Table 3**
Photovoltaic parameters of **PT2**-derived devices.

| Active layer (weight ratio) | $V_{oc}$ (V) | $J_{sc}$ (mA·$cm^{-2}$) | FF (%) | PCE (%) | $R_S$ (Ω $cm^2$) | $R_{SH}$ (Ω $cm^2$) |
|---|---|---|---|---|---|---|
| **PT2-DCN**/$PC_{61}BM$[a] | 0.43 | 2.3 | 39.6 | 0.36 | 87 | 394 |
| **PT2-DCN**/$PC_{61}BM$[b] | 0.42 | 2.4 | 40.0 | 0.40 | 52 | 350 |
| **PT2-DE**/$PC_{61}BM$[a] | 0.81 | 1.5 | 32.0 | 0.39 | 223 | 797 |
| **PT2-DE**/$PC_{61}BM$[b] | 0.77 | 6.3 | 54.7 | 2.64 | 3.9 | 1082 |
| **PT2-DE**/$PC_{71}BM$[b] | 0.73 | 6.3 | 50.4 | 2.31 | 4.3 | 704 |
| **PT2-DAM**/$PC_{61}BM$[a] | 0.39 | 1.0 | 33.5 | 0.12 | 233 | 655 |
| **PT2-DAM**/$PC_{61}BM$[b] | 0.33 | 0.5 | 33.0 | 0.05 | 431 | 111 |

[a] p-type/n-type ratio of 1/1.5.
[b] With DIO additive (1.5%).

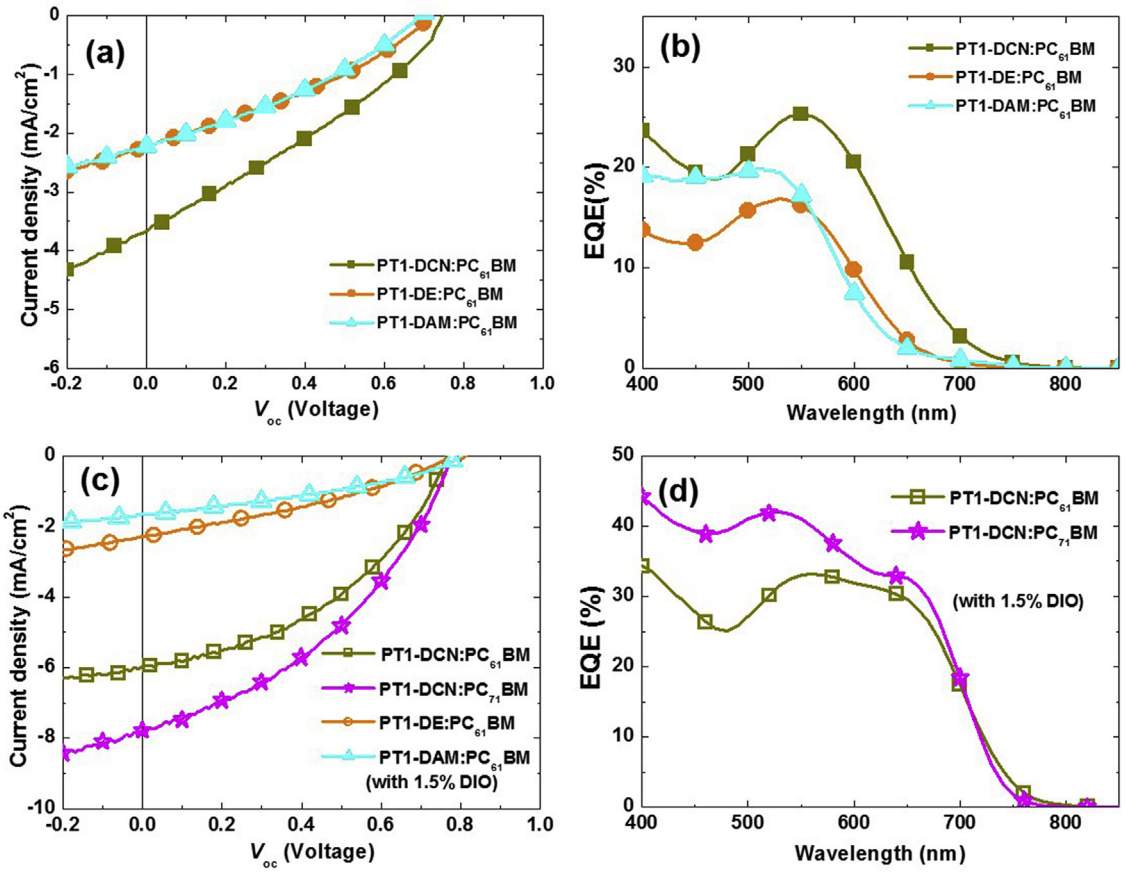


**Fig. 5.** *J-V* curves and EQE responses of the **PT1**-based OPVs devices.

bandgap. Fig. 5b illustrates the IPCE response of the devices. For the **PT1-DE** and **PT1-DAM** devices, the IPCE response occurred at wavelengths 400–700 nm, whereas that for the **PT1-DCN** device was in the range 400–750 nm. These intensities and IPCE responses are consistent with the corresponding $J_{sc}$ and UV–vis spectra. When a small amount of additive (DIO) was added, we observed a significant improvement in the PCE of the **PT1-DCN**/$PC_{61}BM$ devices. This phenomenon was not observed in the **PT1-DE** and **PT1-DAM** devices. The PCE of the **PT1-DCN**/$PC_{61}BM$ device improved from 0.85% to 1.97% because of the significant increase in $J_{sc}$ and FF. The PCE further improved to 2.42% when we replaced the $PC_{61}BM$ with $PC_{71}BM$. Fig. 5d illustrates the IPCE of **PT1-DCN**/$PC_{61}BM$ in the presence of the 1.5 vol% of DIO; the IPCE was increased in the range 400–750 nm compared with the normal device. The IPCE increase from 650 to 750 nm suggested efficient π–π molecular packing in the **PT1-DCN** SMs. Comparing the $PC_{61}BM$ device with the $PC_{71}BM$ device revealed a significant improvement in IPCE from 400 to 600 nm, primarily because of the light harvesting of $PC_{71}BM$ at visible wavelengths. The PCEs of **PT2-DCN**/$PC_{61}BM$, **PT2-DE**/$PC_{61}BM$, and **PT2-DAM**/$PC_{61}BM$ were 0.36%, 0.39%, and 0.12%, respectively. We observed the highest $J_{sc}$ for the **PT2-DCN** device; this value is consistent with the lower energy bandgap (from UV–vis spectrum) and IPCE result (Figs. 3 and 6b). When we added a small amount of additive (DIO), we observed a significant improvement in the PCE of the **PT2-DE**/$PC_{61}BM$ device. This phenomenon was not observed for the **PT2-DCN** and **PT2-DAM** devices. The PCE of the **PT2-DE**/$PC_{61}BM$ device improved from 0.36% to 2.64% in the presence of DIO because of the significant increase in $J_{sc}$ and FF. We observed a similar PCE of 2.31% for the **PT2-DE**/$PC_{71}BM$ device. These performance differences were due to the different solubility of the **PT**-series materials in the DIO.

To determine the changes in film morphology when using DIO as an additive, we performed tapping-mode atomic force microscopy (AFM). Fig. 7a–c present the AFM images of the **PT1-DCN** BHJ films. From the topographical images, we determined the arithmetical mean surface roughness (Ra) of the **PT1-DCN**/$PC_{61}BM$, **PT1-DCN**/$PC_{61}BM$(DIO), and **PT1-DCN**/$PC_{71}BM$ (DIO) blend films to be 0.83, 3.97, and 5.51 nm, respectively. The surface of **PT1-DCN**/$PC_{61}BM$ was featureless and exhibited a very small surface roughness, which may be due to the well-mixed **PT1-DCN** and $PC_{61}BM$. The high surface roughnesses obtained may have been due to the crystallization of **PT1-DCN** molecules. This phenomenon was significant for the **PT2-DE** blend film. The Ra of **PT2-DE**/$PC_{61}BM$ and **PT2-DE**/$PC_{71}BM$ was 0.318 and 0.274 nm, respectively, and increased to 18.1 and 19.6 nm in the presence of DIO. A grain size greater than 1 μm was determined for the **PT2-DE**-rich domains. Typically, a well-defined blend morphology is required for a highly efficient OPV device; the domain sizes of the donor and acceptor need to be segregated on the nanoscale. In this study, we observed microscale segregation of the **PT2-DE**:fullerene blend film with 1.5 vol% of DIO, which resulted in high OPV performance. This phenomenon is not common; we speculate that the carrier mobility in the normal **PT2-DE** devices (w/o DIO) is low, despite the nanoscale blend film morphology. The incorporation of DIO may significantly increase the carrier mobility; we obtained a high PCE even for microscale phase segregation.

To understand the cause of the differences in device performance, we performed hole-only space charge limited current (SCLC) measurements for devices having the configuration ITO/PEDOT:PSS/**PT**-SMs/$MoO_3$/Ag [40,42]. The SCLC hole mobility of

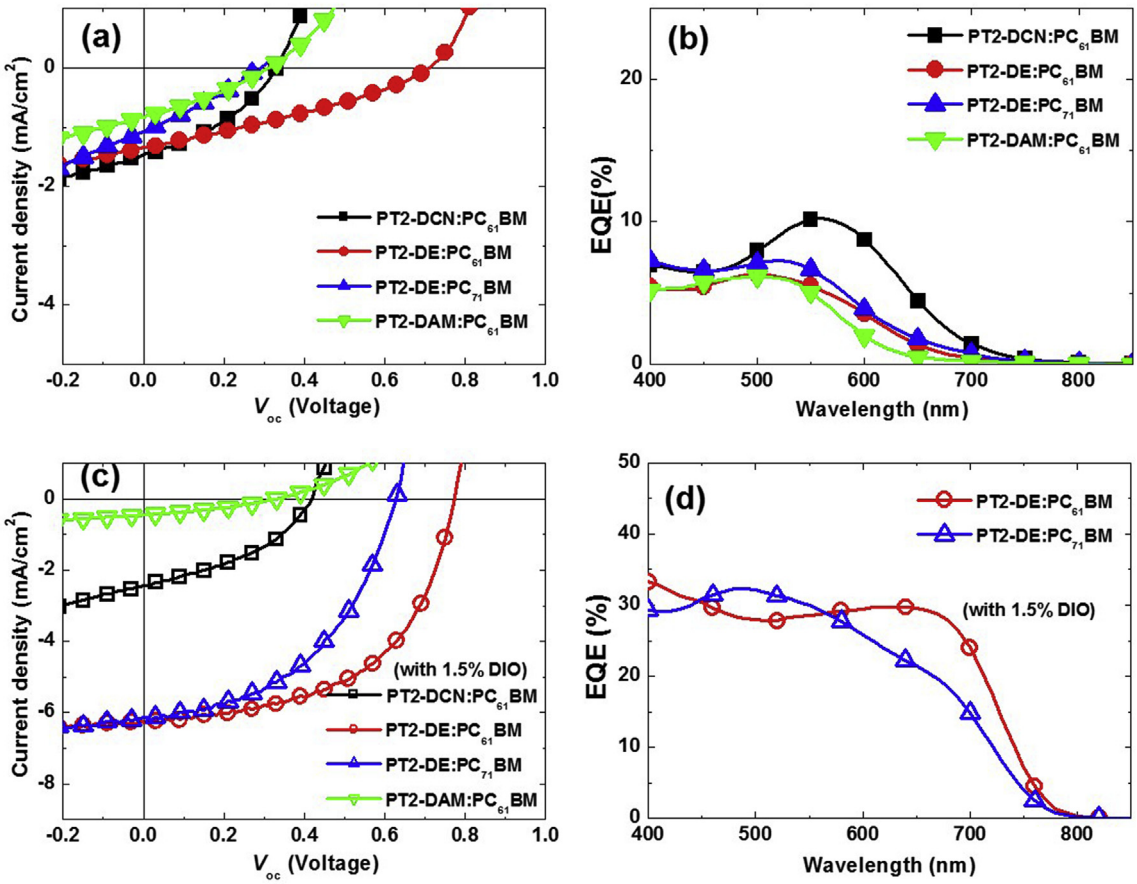


**Fig. 6.** *J-V* curves and EQE of the SMOPVs devices of **PT2**-series with $PC_{61}BM$ and $PC_{71}BM$ as active layer.

**PT1-DE**, **PT1-DAM**, and **PT1-DCN** was $7.5 \times 10^{-10}$, $9.5 \times 10^{-11}$, and $3.9 \times 10^{-9}$ $m^2$ $V^{-1}$ $s^{-1}$, respectively. The highest SCLC hole mobility was obtained for the PT1-DCN devices; this result is consistent with their higher PCE performance. To investigate the cause of the increase in device PCE in the presence of DIO, we further fabricated SCLC devices based on the **PT1-DCN** blend films. The hole mobility of **PT1-DCN**:$PC_{61}BM$ and **PT1-DCN**:$PC_{71}BM$ was $1.3 \times 10^{-10}$ and $3.2 \times 10^{-9}$ $m^2$ $V^{-1}$ $s^{-1}$, respectively. In the presence of DIO, we observed increases in the SCLC hole mobility for **PT1-DCN**:$PC_{61}BM$ ($2.5 \times 10^{-10}$ $m^2$ $V^{-1}$ $s^{-1}$) and **PT1-DCN**:$PC_{71}BM$ ($6.5 \times 10^{-9}$ $m^2$ $V^{-1}$ $s^{-1}$). These results suggest that DIO modified the blend film morphology, increasing hole transport efficiency; thus, we observed an enhancement in the PCE of the devices. The SCLC mobility of the pristine **PT2-DCN**, **PT2-DE,** and **PT2-DAM** was $3.3 \times 10^{-10}$, $2.3 \times 10^{-10}$, and $2.2 \times 10^{-10}$ $m^2$ $V^{-1}$ $s^{-1}$, respectively. We observed similar mobility for materials that exhibited similar OPV device performance. The hole mobility of devices based on **PT2-DE** blend films was $4.6 \times 10^{-11}$ and $1.1 \times 10^{-11}$ $m^2$ $V^{-1}$ $s^{-1}$ for the $PC_{61}BM$- and $PC_{71}BM$-based blends, respectively. Again, we observed an increase in the hole mobility after the addition of DIO; the mobility of devices increased to $4.4 \times 10^{-9}$ and $7.1 \times 10^{-10}$ $m^2$ $V^{-1}$ $s^{-1}$ for the $PC_{61}BM$ and $PC_{71}BM$ blends, respectively. The main factor that determined the carrier mobility was presumably the differences in the morphologies of the active layers; in this case, these differences were due to superior molecular packing (Fig. 7). To confirm this, we performed grazing incidence X-ray diffraction (XRD) analysis and studied the UV–vis spectra of the related blend films. The XRD patterns of **PT2-DE**:$PC_{61}BM$ are shown in Fig. 8a. The blend film without DIO exhibited an amorphous characteristic and a broader peak at the 2θ between 15° and 25°. We observed an increase in the structural ordering of the **PT2-DE**:$PC_{61}BM$ blend in the presence of DIO. The **PT2-DE** molecules showed a strong (100) reflection peak at $2\theta = 4.4°$ corresponding to a $d$ [100]-spacing of 20.0 Å. This value indicated the efficient π–π packing of the **PT2-DE** molecules when the blend film was formed from the DIO-containing solution. This distance covers the range between the coplanar of the phenothiazine main chains of **PT2-DE** separated by the flexible side chains. Fig. 8b presents the UV–vis spectra of the blend films. A red-shift of 150 nm was observed in the spectra of the blend films when DIO had been added, indicating highly organized **PT2-DE** molecules in the solid state. Large-scale phase-segregation morphology was observed for the **PT2-DE**–DIO blend films because of the crystalline-grain-sized increase in the **PT2-DE** molecules; therefore, we obtained an improvement of greater than one order of magnitude in the SCLC hole mobility. As a result, a 5-fold increase in the PCE of the PT2-DE-based OPV devices was determined. We observed similar phenomena for the **PT1-DCN** blend film. In the presence of DIO, the **PT1-DCN** film exhibited a strong (100) reflection peak at $2\theta = 5°$, a (200) reflection peak at $2\theta = 10°$, and a (300) reflection peak at 15°, indicating the ordering structure in the blend and again a red-shift in the UV–vis spectrum. The performance of the **PT1-DCN**–based device increased because of a significant improvement in the mobility. In the future, we expect to further increase the performance of phenothiazine-based materials through optimized device engineering. Determining the order of molecular orientation (from variations in materials and blend system to variations in device engineering) can be challenging; our

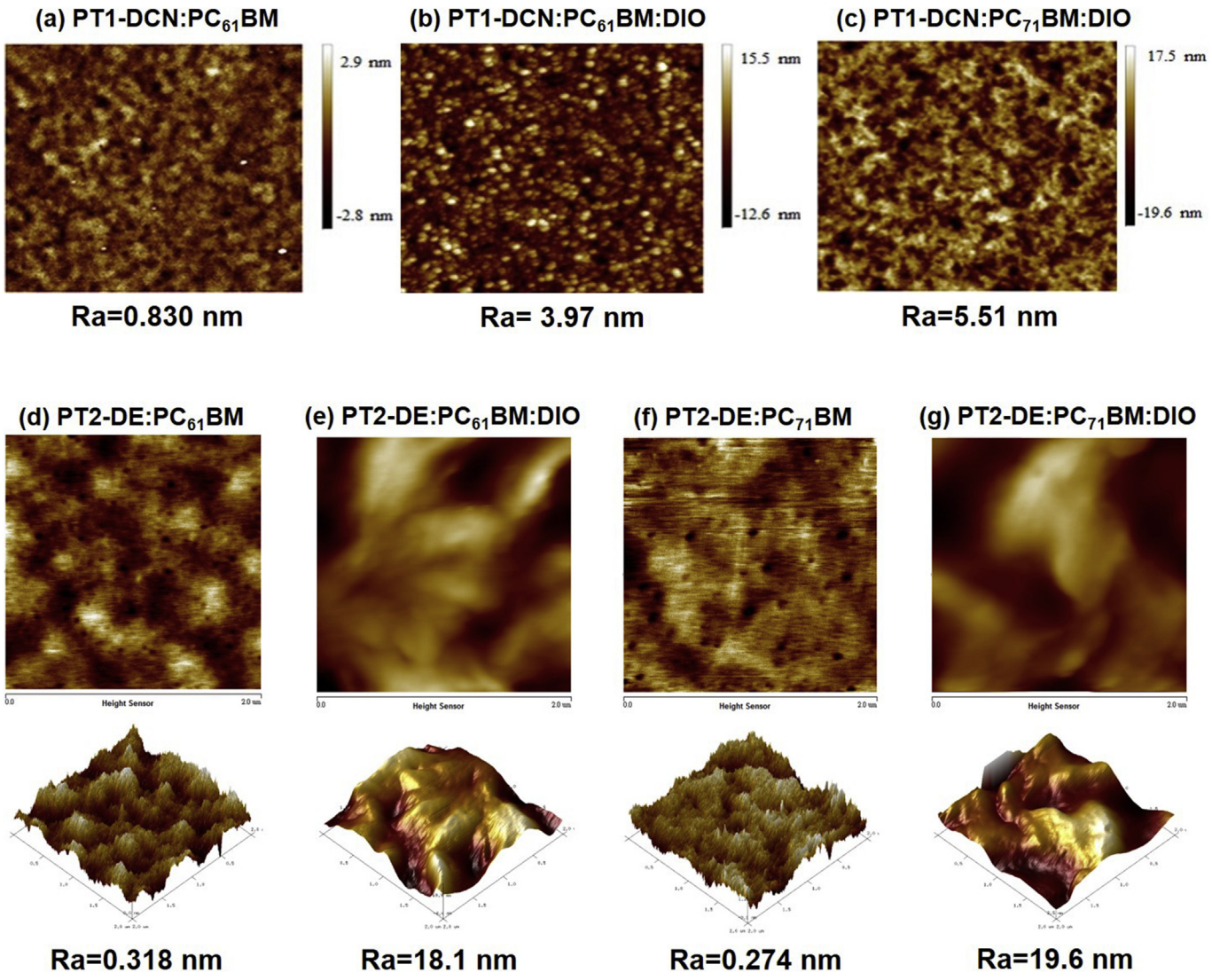


**Fig. 7.** AFM (a) **PT1-DCN**/$PC_{61}BM$; (b) **PT1-DCN**/$PC_{61}BM$/DIO; (c) **PT1-DCN**/$PC_{71}BM$/DIO; (d) **PT2-DE**/$PC_{61}BM$; (e) **PT2-DE**/$PC_{61}BM$/DIO; (f) **PT2-DE**/$PC_{71}BM$; (g) **PT2-DE**/$PC_{71}BM$/DIO. (2 μm × 2 μm).

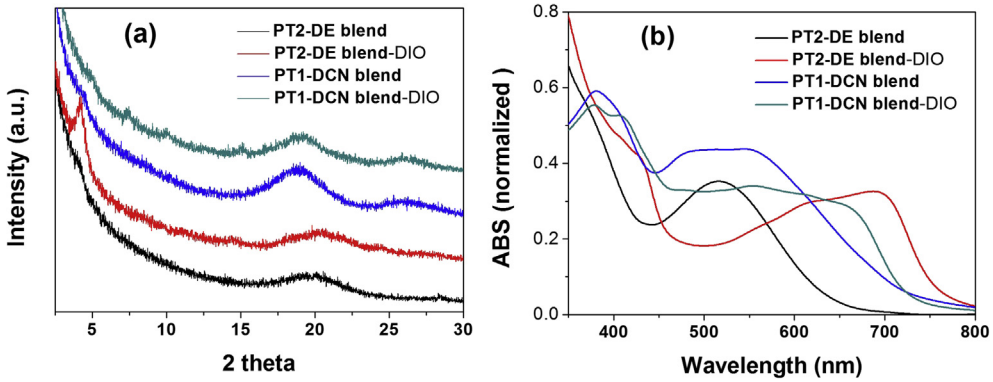


**Fig. 8.** a) XRD patterns and b) UV–vis spectra of the **PT2-DE** and **PT1-DCN** based blend films in the presence of and without the DIO.

XRD data confirmed the enhancement in the molecular order for the blend films in the presence of DIO and we observed improvement in the device performance (PCE and hole mobility). Further understanding the molecular arrangement and self-assembly behavior of these phenothiazine-based materials has been carried out in the laboratory. By effective controlling the molecular packing of these materials will have the opportunity to further improve the device performance.

## 3. Conclusion

In summary, we demonstrated that **PT**-series p-type materials utilize phenothiazine moieties as electron-donating (D) groups with three different acceptors (dicyanovinyl, ethyl 2-cyanoacrylate, and 2-cyano-*N*-hexylacrylamide) by employing A–D–A and A–D–D–A dipolar systems as the p-type materials in photovoltaic solar cells. By substituting different molecules as the A unit, we obtained molecules with various optoelectronic properties.

A well-defined blend morphology is required for a highly efficient OPV device; the domain sizes of the donor and acceptor need to be segregated on the nanoscale. In this study, we observed microscale segregation of the **PT2-DE**:fullerene blend film with 1.5 vol% of DIO, which resulted in high OPV performance. Incorporating **PT2-DE**/$PC_{61}BM$ in an OPV cell with the additive DIO resulted in a PCE of 2.64% and $V_{oc}$ was 0.77 V, $J_{sc}$ was 6.3 mA $cm^{-2}$, and the FF was 54.7%; the PCE was thus increased 5-fold when DIO was added. This improvement was due to the superior π–π molecular packing in the **PT2-DE** (as determined using XRD) and resulted in a one-order-of-magnitude increase in hole mobility. We also observed a similar PCE of 2.31% for the **PT2-DE**/$PC_{71}BM$ device. Because of differences in the solubility of the **PT** materials in DIO, the performance of the devices varied.

## 4. Experimental section

### 4.1. General information

All reactions and manipulations were performed in a nitrogen atmosphere. Solvents were distilled freshly according to standard procedures. $^1H$ and $^{13}C$ NMR spectra were recorded on a Bruker AVIII HD 400 MHz spectrometer, and $CDCl_3$ was used as solvents. Chemical shifts were reported on the **δ** scale downfield from the tetramethylsilane peak. Absorption spectra were recorded on a SHIMADZU UV-1800 and Jasco V-630 spectrophotometer, and emission spectra were obtained using a Hitachi F-4500 spectrofluorimeter. Emission spectra in solutions were measured using a spectral grade solvent and right-angle detection. Redox potentials were measured using cyclic voltammetry on a CHI 620 analyser. All measurements were performed in THF solution containing 0.1 M tetrabutylammonium hexaflourophosphate as a supporting electrolyte in ambient conditions after purging the solution with $N_2$ for 10 min. The conventional three-electrode configuration, consisting of a glassy carbon working electrode, a platinum counter electrode, and an $Ag/Ag^+$ reference electrode calibrated with ferrocene/ferrocenium ($Fc/Fc^+$) as an internal reference, was employed. Mass spectra were recorded on a JEOL JMS-700 double-focusing mass spectrometer. The surface morphology of the materials was characterized by the non-contact mode atomic force microscopy (Bruker Dimension Edge microscope operated in the dynamic force mode at ambient temperature.). Thermogravimetric analysis (TGA; Pyris 1 TGA Lab system) measurements were carried out with heating rate of 10 °C/min under a nitrogen gas atmosphere.

The chemicals *N*-Bromosuccinimide (NBS), *trans*-Dichlorobis(-triphenylphosphine) palladium(II) ($PdCl_2(PPh_3)_2$), Dichloromethane, tetrakis(triphenylphosphine)palladium(0) (P d($PPh_3)_4$), n-Butyllithium (1.6 M in hexane), Triisopropyl borate *N,N′*-Dimethylformamide, Malononitrile, Ethyl cyanoacetate, 2-Cyano-*N*-hexylacetamide, Ammonium acetate, Tetrahydrofuran, Toluene, and Piperidine were purchased from Acros, Alfa, Merck, Lancaster, TCI, Sigma-Aldrich, and Showa, separately, and purified when necessary. Chromatographic separations were performed using silica gel from Merck (Kieselgel Si 60; 40–63 μm).

### 4.2. Synthesis of PT-series p-type materials

#### 4.2.1. 3,7-Dibromo-10-(4-(dodecyloxy)phenyl)-10H-phenothiazine (2)

A mixture of **1** (5.0 g, 10.8 mmol) in dry $CH_2Cl_2$ was placed in a three-necked flask under a nitrogen atmosphere. Following this, added dropwise NBS (3.84 g, 21.6 mmol) in $CH_2Cl_2$ to this reaction and stirred 6 h room temperature. The mixture was quenched by adding DI water, and the mixture extracted with $CH_2Cl_2$. The organic layer was dried over anhydrous $MgSO_4$ and evaporated under vacuum. The product was purified by silica gel column chromatograph with hexane as eluent. Yellow solid of **2** was obtained in 97% yield (6.5 g, 10.5 mmol). $^1H$ NMR (400 MHz, $CDCl_3$): δ 7.22 (d, 2H, *J* = 8.8 Hz), 7.09 (d, 2H, *J* = 8.8 Hz), 7.07 (d, 2H, *J* = 2.2 Hz), 6.90 (dd, 2H, *J* = 8.8, 2.2 Hz), 6.01 (d, 2H, *J* = 8.8 Hz), 4.02 (t, 2H, *J* = 6.5 Hz), 1.80–1.86 (m, 2H), 1.46–1.51 (m, 2H), 1.27–1.36 (m, 16H), 0.88 (t, 3H, *J* = 6.8 Hz). $^{13}C$ NMR (100 MHz, $CDCl_3$): δ 159.2, 143.5, 132.2, 131.7, 129.7, 128.7, 121.0, 116.9, 116.7, 114.5, 68.4, 31.9, 29.7, 29.6, 29.6, 29.5, 29.4, 29.3, 29.2, 26.1, 26.7, 14.1. MS (FAB, 70 eV): *m*/*z* (relative intensity) 615 ($M^+$, 100); HRMS calcd for $C_{30}H_{35}NOS^{79}Br_2$: 615.0806, found 615.0818.

#### 4.2.2. 5,5′-(10-(4-(Dodecyloxy)phenyl)-10H-phenothiazine-3,7-diyl)bis(thio phene-2-carbaldehyde) (3)

To a three-necked flask containing a mixture of **2** (5.0 g, 8.1 mmol), $PdCl_2(PPh_3)_2$ (190 mg, 0.25 mmol), (5-(1,3-dioxolan-2-yl)thiophen-2-yl) tributylstannane (4.0 g, 9.0 mmol) was added DMF (50 mL). The reaction mixture was stirred at 90 °C for 24 h. After cooling, the reaction was quenched by adding methanol and $KF_{(aq)}$ (saturated 45 mL). Evaporation of the solvent gave a crude product. The crude mixture was added Acetic acid/THF/de-ionized water (40/20/10 mL) at 60 °C. After 3 h, the reaction was quenched by adding de-ionized water and brine. The mixture was extracted with $CH_2Cl_2$ and the organic layer dried over anhydrous $MgSO_4$. Evaporation of the solvent gave the crude, which was purified by silica gel with $CH_2Cl_2$ as eluent. Red solid of **3** was obtained in 63.6% (3.5 g, 5.1 mmol). $^1H$ NMR (400 MHz, $CDCl_3$): δ 9.75 (s, 2H), 7.58 (d, 2H, *J* = 3.8 Hz), 7.12–7.18 (m, 6H), 7.08 (d, 2H, *J* = 8.72 Hz), 7.01 (d, 2H, *J* = 8.8 Hz), 6.08 (d, 2H, *J* = 8.6 Hz), 4.00 (t, 2H, *J* = 6.36 Hz), 1.79–1.83 (m, 2H), 1.45–1.49 (m, 2H), 1.28–1.31 (m, 16H), 0.87 (t, 3H, *J* = 6.36). $^{13}C$ NMR (100 MHz, $CDCl_3$): δ 182.2, 159.1, 152.7, 144.1, 141.3, 137.4, 131.6, 131.3, 127.3, 125.0, 123.7, 122.8, 119.5, 116.6, 115.9, 68.2, 31.7, 29.5, 29.4, 29.3, 29.1, 29.0, 25.9, 22.5, 14.0. MS (FAB, 70 eV): *m*/*z* (relative intensity) 679 ($M^+$, 100); HRMS calcd for $C_{40}H_{41}NO_3S_3$: 679.2249, found 679.2245.

#### 4.2.3. 3-Bromo-10-(4-(dodecyloxy)phenyl)-10H-phenothiazine (4)

Compound **4** was synthesized according to the same procedure as that of **2**. Yellow solid was obtained in 46% yield. $^1H$ NMR (400 MHz, $CDCl_3$): δ 7.24 (d, 2H, *J* = 8.12 Hz), 7.07–7.11 (m, 3H), 6.96 (dd, 1H, *J* = 7.24, 1.94 Hz), 6.89 (dd, 1H, *J* = 8.8, 2.2 Hz), 6.76–6.85 (m, 2H), 6.18 (dd, 1H, *J* = 7.96, 1.4 Hz), 6.02 (d, 2H, *J* = 8.8 Hz), 4.02 (t, 2H, *J* = 6.5 Hz), 1.80–1.87 (m, 2H), 1.46–1.52 (m, 2H), 1.28–1.31 (m, 16H), 0.89 (t, 3H, *J* = 6.9 Hz). $^{13}C$ NMR (100 MHz, $CDCl_3$): δ 159.0, 144.3, 143.9, 132.6, 132.0, 129.4, 128.6, 127.1, 126.6, 122.5, 121.8, 118.8, 116.8, 116.8, 116.5, 115.7, 114.168.4, 31.9, 29.7, 229.6, 29.5, 29.4, 29.4, 29.3, 26.1, 22.7, 14.1. MS (FAB, 70 eV): *m*/*z* (relative intensity) 537 ($M^+$, 100); HRMS calcd for $C_{30}H_{36}NOS^{79}Br$: 537.1701, found 537.1691.

#### 4.2.4. 10,10′-Bis(4-(dodecyloxy)phenyl)-10H,10′H-3,3′-biphenothiazine (5)

To a three-necked round-bottom flask containing **4** (2.5 g,

4.6 mmol) was added dropwise BuLi (5.0 mL, 8.0 mmol, 1.6 M in hexane) in dry THF at −78 °C, after then the solution was brought up to 0 °C and was stirred by a magnetic bar for 30 min. The solution was cooled again to −78 °C and to it was added dropwise triisopropyl borate (2.2 mL, 8.0 mmol). The reaction was warmed up gradually to room temperature and was stirred overnight. To the reaction was then added excess amount of 10% $HCl_{(aq)}$ (30 mL), while the mixture was stirred for another 1 h. The reaction was quenched by pouring into distilled water, followed by extraction with ethyl acetate. The organic layer was dried over anhydrous $MgSO_4$. Evaporation of the solvent gave a crude product, which was immediately subjected to the next reaction. It was mixed with **4** (2.5 g, 4.6 mmol), $K_2CO_{3(aq)}$ (2.76 g, 2 mmol) in 10 mL $H_2O$, and $Pd(PPh_3)_4$ (190 mg, 0.16 mmol) in dry toluene/THF (2/1). The mixture was heated to 60 °C for 12 h. After cooling, the products were extracted with ethyl acetate and the organic layer dried over anhydrous $MgSO_4$. The crude product was dried *in vacuo*, and was purifies by silica gel column chromatograph eluted with $CH_2Cl_2$/hexane (1/8). Yellow solid of **5** was obtained in 72% yield (3.1 g, 3.3 mmol). $^1$H NMR (400 MHz, $CDCl_3$): $\delta$ 7.29 (d, 4H, $J$ = 8.72 Hz), 7.11–7.09 (m, 6H), 6.99 (d, 6H, $J$ = 7.0 Hz), 6.84–6.81 (m, 4H), 6.19 (d, 4H, $J$ = 7.9 Hz), 4.03 (t, 4H, $J$ = 6.5 Hz), 1.87–1.80 (m, 4H), 1.52–1.46 (m, 4H), 1.40–1.28 (m, 32H), 0.91 (t, 6H, $J$ = 6.4 Hz); $^{13}$C NMR (100 MHz, $CDCl_3$): $\delta$ 158.9, 143.6, 134.0, 132.9, 132.1, 126.8, 126.6, 124.5, 124.1, 122.2, 120.0, 119.2, 116.4, 115.8, 115.6, 77.3, 77.0, 76.7, 68.3, 31.9, 29.7, 29.6, 29.6, 29.4, 29.3, 29.3, 26.1, 22.7, 14.1. MS (FAB, 70 eV): $m/z$ (relative intensity) 916 ($M^+$, 100); HRMS calcd for $C_{60}H_{72}N_2O_2S_2$: 916.5035, found 916.5020.

#### 4.2.5. 7,7′-Dibromo-10,10'-bis(4-(dodecyloxy)phenyl)-10H,10′H-3,3'-biphenothiazine (6)

Compound **6** was synthesized according to the same procedure as that of **2**. Yellow solid of **6** was obtained in 86% yield. $^1$H NMR (400 MHz, $CDCl_3$): $\delta$ 7.22–7.25 (m, 4H), 7.05–7.10 (m, 8H), 6.88 (dd, 4H, $J$ = 2.06 Hz, 8.78 Hz), 6.15 (d, 2H, $J$ = 8.5 Hz), 6.01 (d, 2H, $J$ = 8.6 Hz), 4.02 (t, 4H, $J$ = 6.4 Hz), 1.81–1.85 (m, 4H), 1.46–1.51 (m, 4H), 1.28–1.38 (m, 32H), 0.89 (t, 6H, $J$ = 6.6 Hz). $^{13}$C NMR (100 MHz, $CDCl_3$): $\delta$ 159.0, 143.6, 1432, 134.0, 132.5, 131.9, 129.4, 128.6, 124.8, 124.1, 121.4, 119.2, 116.8, 116.5, 115.9,114.2, 68.4, 31.9, 29.7, 29.6, 29.6, 29.5, 29.4, 29.3, 29.3, 26.1, 22.7, 14.1. MS (FAB, 70 eV): $m/z$ (relative intensity) 1072 ($M^+$, 100); HRMS calcd for $C_{60}H_{70}Br_2N_2O_2S_2$: 1072.3245, found 1072.3219.

#### 4.2.6. 5,5'-(10,10′-Bis(4-(dodecyloxy)phenyl)-10H,10′H-[3,3'-bipheno-thiazine]-7,7'-diyl)bis(thiophene-2-carbaldehyde) (7)

Compound **7** was synthesized according to the same procedure as that of **3**. Yellow solid of **7** was obtained in 42% yield. $^1$H NMR (400 MHz, $CDCl_3$): $\delta$ 9.82 (s, 2H),7.65 (dd, 2 H, $J$ = 0.78 Hz, 3.89 Hz) 7.24–7.27 (m, 6H), 7.21 (s, 1H), 7.20 (s, 1H), 7.08–7.12 (m, 8H), 6.89 (d, 2H, $J$ = 7.84 Hz), 6.16 (dd, 4H, $J$ = 4.06 Hz, 8.34 Hz), 4.03 (t, 4H, $J$ = 6.4 Hz), 1.87–1.81 (m, 4H), 1.55–1.47 (m, 4H), 1.4–1.28 (m 32H), 0.89 (t, 6H, $J$ = 6.4 Hz); $^{13}$C NMR (100 MHz, $CDCl_3$): $\delta$ 182.4, 159.1, 153.3,145.1, 142.6, 141.4, 137.5, 134.2, 131.7, 127.1, 125.1, 124.7, 124.0, 122.8, 120.0, 119.2, 116.6, 116.1, 115.7, 68.4, 31.9, 29.6, 29.6, 29.6, 29.4, 29.3, 29.2, 26.1, 22.7, 14.1; MS (FAB, 70 eV): $m/z$ (relative intensity) 1136 ($M^+$, 100); HRMS calcd for $C_{70}H_{76}N_2O_4S_4$: 1136.4688, found 1136.4645.

#### 4.2.7. 2,2'-(((10-(4-(Dodecyloxy)phenyl)-10H-phenothiazine-3,7-diyl) bis(thiophene-5,2-diyl))bis-(methanylylidene))dimalononitrile (PT1-DCN)

A mixture of **3** (0.5 g, 0.7 mmol), NH4Oac (0.1 g, 13 mmol), and malononitrile (0.2 g, 3.0 mmol) were placed in a three-necked flask containing dry toluene (20 mL) under $N_2$. The resulted mixture was heated to reflux for 24 h. After cooling, the reaction was quenched by pouring into water and it was extracted with $CH_2Cl_2$. The combined organic layer was dried over anhydrous $MgSO_4$ and evaporated under vacuum. The mixture was purified by silica gel column chromatograph with $CH_2Cl_2$ as eluent. The black solid of **PT1-DCN** was collected in 81% yield (0.47 g, 0.6 mmol). $^1$H NMR (400 MHz, $CDCl_3$): $\delta$ 8.25 (s, 2H), 7.68 (d, 2 H, $J$ = 4.12 Hz) 7.24–7.28 (m, 2H), 7.14 (d, 4H, 8.6 Hz), 7.13 (d, 4H, $J$ = 8.8 Hz), 6.16 (d, 2H, $J$ = 8.6 Hz), 4.05 (t, 2H, $J$ = 6.5 Hz), 1.82–1.89 (m, 2H), 1.28–1.38 (m 22H), 089 (t, 6H, $J$ = 6.6 Hz); $^{13}$C NMR (100 MHz, $CDCl_3$): $\delta$ 159.5, 155.2, 150.2, 144.9, 140.1, 133.5, 131.5, 131.3, 127, 125.7, 124.2, 123.6, 119.9, 116.9, 116.3, 114.3, 113.5, 75.8, 68.5, 31.9, 29.6, 29.6, 29.6, 29.4, 29.3, 29.2, 26.0, 22.7, 14.1; MS (FAB, 70 eV): $m/z$ (relative intensity) 775 ($M^+$, 100); HRMS calcd for $C_{46}H_{41}N_5OS_3$: 775.2473, found 775.2473.

#### 4.2.8. Diethyl 3,3'-((10-(4-(dodecyloxy)phenyl)-10H-phenothiazine-3,7-diyl)bis(thiophene-5,2-diyl))(2E,2′E)-bis(2-cyanoacrylate) (PT1-DE)

Compound **PT1-DE** was synthesized according to the same procedure as that of **PT1-DCN**. Red solid of **PT1-DE** was obtained in 83% yield. $^1$H NMR (400 MHz, $CDCl_3$): $\delta$ 8.25 (s, 2H),7.68 (d, 2 H, 4.12 Hz), 7.24–7.28 (m, 6H), 7.13 (dd, 4H, $J$ = 8.76, 1.96 Hz), 6.16 (d, 2H, $J$ = 8.6 Hz), 4.35 (q, 4H, $J$ = 7.15 Hz), 4.05 (t, 2H, $J$ = 6.5 Hz), 1.82–1.89 (m, 2H), 1.28–1.38 (m 22H), 089 (t, 6H, $J$ = 6.6 Hz); $^{13}$C NMR (100 MHz, $CDCl_3$): $\delta$ 163.0, 159.4, 153.3, 146.3, 144.4, 139.2, 134.1, 1317, 131.4, 127.3, 125.3, 124.0, 123.3, 119.8, 116.8, 116.1, 97.3, 68.4, 62.3, 31.9, 29.6, 29.6, 29.9, 29.4, 29.3, 29.2, 26.0, 22.6, 14.2, 14.1. MS (FAB, 70 eV): $m/z$ (relative intensity) 869 ($M^+$, 100); HRMS calcd for $C_{50}H_{51}N_3O_5S_3$: 869.2991, found 869.2986.

#### 4.2.9. (2E,2′E)-3,3'-((10-(4-(Dodecyloxy)phenyl)-10H-phenothiazine-3,7-diyl)bis(thiophene-5,2-diyl))bis-(2-cyano-N-hexylacrylamide) (PT1-DAM)

Compound **PT1-DAM** was synthesized according to the same procedure as that of **PT1-DCN**. Red solid of **PT1-DAM** was obtained in 62% yield. $^1$H NMR (400 MHz, $CDCl_3$): $\delta$ 8.23 (s, 2H), 7.60 (d, 2 H, $J$ = 4.08 Hz), 7.25–7.27 (m, 4H), 7.22 (d, 2 H, $J$ = 4.04 Hz), 7.10–7.14 (m, 4H), 6.23 (t, 2H, $J$ = 5.68 Hz), 6.15 (d, 2H, $J$ = 8.6 Hz), 4.04 (t, 2H, $J$ = 6.48 Hz), 3.40 (q, 4H, $J$ = 6.92 Hz), 1.81–1.88 (m, 2H), 1.47–1.62 (m, 6H), 1.28–1.38 (m, 28H), 0.86–0.91 (m, 9H); $^{13}$C NMR (100 MHz, $CDCl_3$): $\delta$ 160.6, 159.3, 151.9, 144.4, 144.4, 144.3, 138.4, 134.6, 131.8, 1315, 127.5, 125.3, 124.0, 123.2, 119.8, 117.5, 116.7, 116.1, 98.8, 68.4, 40.5, 31.9, 31.4, 29.6, 29.6, 29.6, 29.4, 29.3, 29.2, 26.5, 26.0, 22.6, 22.5, 14.1, 13.9; MS (FAB, 70 eV): $m/z$ (relative intensity) 979 ($M^+$, 100); HRMS calcd for $C_{58}H_{69}N_5O_3S_3$: 979.4563, found 979.4561.

#### 4.2.10. 2,2'-(((10,10′-Bis(4-(dodecyloxy)phenyl)-10H,10′H-[3,3'-bipheno-thiazine]-7,7'-diyl)bis(thiophene-5,2-diyl)) bis(methanylylidene)) dimalononitrile (PT2-DCN)

Compound **PT2-DCN** was synthesized according to the same procedure as that of **PT1-DCN**. Black solid of **PT2-DCN** was obtained in 70% yield. $^1$H NMR (400 MHz, $CDCl_3$): $\delta$ 7.71 (s, 2H), 7.63 (d, 2 H, $J$ = 4.2 Hz), 7.24–7.26 (m, 8H), 7.12 (d, 6H, $J$ = 8.8 Hz), 7.07 (d, 2H, $J$ = 2.0 Hz), 6.92 (dd, 2H, $J$ = 8.6, 2.4 Hz), 6.16 (dd, 4H, $J$ = 8.6, 2.4 Hz), 4.04 (t, 4H, $J$ = 6.4 Hz), 1.81–1.88 (m, 4H), 1.47–1.54 (m, 4H), 1.28–1.38 (m, 32H), 0.89–0.86 (t, 6H, $J$ = 6.8 Hz); $^{13}$C NMR (100 MHz, $CDCl_3$): $\delta$ 159.3, 155.8, 150.2, 145.9, 142.4, 140.2, 134.4, 133.2, 132.0, 131.6, 126.2, 125.5, 124.8, 124.2, 124.1, 123.3, 120.3, 119.1, 116.7, 116.3, 115.8, 114.4, 113.6, 77.3, 77.2, 77.0, 76.7, 75.4, 68.4, 31.9, 29.7, 29.6, 29.6, 29.6, 29.4, 29.3, 29.2, 26.1, 22.7, 14.1. MS (FAB, 70 eV): $m/z$ (relative intensity) 1232 ($M^+$, 100); HRMS calcd for $C_{76}H_{76}N_6O_2S_4$: 1232.4913, found 1232.4927.

*4.2.11. Diethyl 3,3'-((10,10'-bis(4-(dodecyloxy)phenyl)-10H,10'H-[3,3'-biphenothiazine]-7,7'-diyl)bis(thiophene-5,2-diyl))(2E,2'E)-bis(2-cyanoacrylate) (PT2-DE)*

Compound **PT2-DE** was synthesized according to the same procedure as that of **PT1-DCN**. Black solid of **PT2-DE** was obtained in 56% yield. $^1$H NMR (400 MHz, $CDCl_3$): $\delta$ 8.24 (s, 2H), 7.68 (d, 2H, $J$ = 4.08 Hz), 7.23–7.28 (m, 8H), 7.08–7.14 (m, 8H), 6.93 (dd, 2H, $J$ = 2.0 Hz, 8.6 Hz), 6.17 (dd, 4H, $J$ = 8.6, 3.24 Hz), 4.35 (q, 4H, $J$ = 7.08 Hz), 4.04 (t, 4H, $J$ = 6.44 Hz), 1.82–1.89 (m, 4H), 1.47–1.53 (m, 4H), 1.28–1.40 (m, 38H), 089 (t, 6H, $J$ = 6.96 Hz); $^{13}$C NMR (100 MHz, $CDCl_3$): $\delta$ 163.1, 159.2, 153.8, 146.4, 145.4, 142.6, 139.3, 134.3, 134.0, 132.2, 131.7, 126.8, 125.3, 124.8, 124.1, 123.1, 120.2, 119.2, 116.7, 116.2, 115.7, 97.1, 68.4, 62.3, 31.9, 29.7, 29.6, 29.6, 29.4, 29.3, 29.3, 26.1, 22.7, 14.2, 14.1. MS (FAB, 70 eV): $m/z$ (relative intensity) 1326 ($M^+$, 100); HRMS calcd for $C_{80}H_{86}N_4O_6S_4$: 1326.5430, found 1326.5415.

*4.2.12. (2E,2'E)-3,3'-((10,10'-bis(4-(dodecyloxy)phenyl)-10H,10'H-[3,3'-biphenothiazine]-7,7'- diyl)bis(thiophene-5,2-diyl))bis(2-cyano-N-hexylacrylamide) (PT2-DAM)*

Compound **PT2-DAM** was synthesized according to the same procedure as that of **PT1-DCN**. Red solid of **PT2-DAM** was obtained in 83% yield. $^1$H NMR (400 MHz, $CDCl_3$): $\delta$ 8.31 (s, 2H), 7.60 (d, 2 H, $J$ = 4.08 Hz), 7.26–7.27 (m, 4H), 7.19 (d, 2H, $J$ = 4.0 Hz), 7.08–7.13 (m, 8H), 6.92 (dd, 2H, $J$ = 8.6, 1.72 Hz), 6.22 (t, 2H, $J$ = 5.52 Hz), 6.16 (dd, 4H, $J$ = 8.6, 3.96 Hz), 4.04 (t, 4H, $J$ = 6.36 Hz), 3.40 (q, 4H, $J$ = 6.72 Hz), 1.81–1.88 (m, 4H), 1.47–1.55 (m, 8H), 1.28–1.38 (m, 44H), 0.86–0.88 (m, 12H); $^{13}$C NMR (100 MHz, $CDCl_3$): $\delta$ 160.7, 159.2, 152.4, 145.2, 144.4, 142.6, 138.4, 134.4, 134.3, 132.3, 131.8, 127.0, 125.1, 124.7, 124.1, 124.1, 123.0, 120.1, 119.2, 117.6, 116.6, 116.2, 115.7, 98.6, 68.4, 40.6, 31.9, 31.4, 29.7, 29.6, 29.6, 29.4, 29.3, 29.3, 26.5, 16.1, 22.7, 22.5, 14.1, 14.0; MS (FAB, 70 eV): $m/z$ (relative intensity) 1436 ($M^+$, 100); HRMS calcd for $C_{88}H_{104}N_6O_4S_4$: 1436.7002, found 1436.6996.

### 4.3. Quantum chemistry computations

All organic molecules were optimized by using B3LYP/6-31G* hybrid functional. For excited states, the time-dependent density functional theory (TDDFT) and the B3LYP functional were used. All analyses were performed using the Q-Chem 3.0 software. The frontier orbital plots of the highest and lowest occupied molecular orbitals (hereafter abbreviated as HOMO and LUMO, respectively) were drawn using GaussView 04.

## Acknowledgements

This work was financial supported by the Ministry of Science and Technology of Taiwan (MOST 103-2113-M-029-007-MY2, 105-2119-M-029-001-), Tunghai University, Ming Chi University of Technology and Academia Sinica are gratefully acknowledged. Special thanks to Professor C.-P. Hsu at the Institute of Chemistry Sinica of Taiwan for her assistance on quantum.

## Appendix A. Supplementary data

Supplementary data related to this article can be found at http://dx.doi.org/10.1016/j.dyepig.2017.07.027.

## References

[1] Pastorelli F, Schmidt TM, Hösel M, Søndergaard RR, Jørgensen M, Krebs FC. The organic power transistor: roll-to-roll manufacture, thermal behavior, and power handling when driving printed electronics. Adv Eng Mater 2016;18:51–5.
[2] Emmott CJM, Moia D, Sandwell P, Ekins-Daukes N, Hösel M, Lukoschek L, et al. In-situ, long-term operational stability of organic photovoltaics for off-grid applications in Africa. Sol Energy Mater Sol Cells 2016;149:284–93.
[3] Wang K, Liu C, Meng T, Yi C, Gong X. Inverted organic photovoltaic cells. Chem Soc Rev 2016;45:2937–75.
[4] Yi C, Hu X, Gong X, Elzatahry A. Interfacial engineering for high performance organic photovoltaics. Mater Today 2016;19:169–77.
[5] Li S, Ye L, Zhao W, Zhang S, Mukherjee S, Ade H, et al. Energy-level modulation of small-molecule electron acceptors to achieve over 12% efficiency in polymer solar cells. Adv Mater 2016;28:9423–9.
[6] Zhao J, Li Y, Yang G, Jiang K, Lin H, Ade H, et al. Efficient organic solar cells processed from hydrocarbon solvents. Nat Energy 2016;1:15027.
[7] Lu L, Zheng T, Wu Q, Schneider AM, Zhao D, Yu L. Recent advances in bulk heterojunction polymer solar cells. Chem Rev 2015;115:12666–731.
[8] Zhang S, Ye L, Hou J. Breaking the 10% efficiency barrier in organic photovoltaics: morphology and device optimization of well-known PBDTTT polymers. Adv Energy Mater 2016;6:1502529.
[9] Collins SD, Ran NA, Heiber MC, Nguyen T-Q. Small is powerful: recent progress in solution-processed small molecule solar cells. Adv Energy Mater 2017;7.1602242.
[10] Kan B, Li M, Zhang Q, Liu F, Wan X, Wang Y, et al. A series of simple oligomer-like small molecules based on oligothiophenes for solution-processed solar cells with high efficiency. J Am Chem Soc 2015;137:3886–93.
[11] Zhang Q, Kan B, Liu F, Long G, Wan X, Chen X, et al. Small-molecule solar cells with efficiency over 9%. Nat Phot 2015;9:35–41.
[12] Sim J, Lee H, Song K, Biswas S, Sharma A, Sharma GD, et al. Solution processed bulk heterojunction solar cells based on A-D-A small molecules with a dihydroindoloindole (DINI) central donor and different acceptor end groups. J Mater Chem C 2016;4:3508–16.
[13] Chung C-L, Chen C-Y, Kang H-W, Lin H-W, Tsai W-L, Hsu C-C, et al. A–D–A type organic donors employing coplanar heterocyclic cores for efficient small molecule organic solar cells. Org Electron 2016;28:229–38.
[14] Vegiraju S, Hsieh C-M, Huang D-Y, Chen Y-C, Priyanka P, Ni J-S, et al. Synthesis and characterization of solution-processable diketopyrrolopyrrole (DPP) and tetrathienothiophene (TTA)-based small molecules for organic thin film transistors and organic photovoltaic cells. Dyes Pigments 2016;133:280–91.
[15] Li Z, Dong Q, Li Y, Xu B, Deng M, Pei J, et al. Design and synthesis of solution processable small molecules towards high photovoltaic performance. J Mater Chem 2011;21:2159–68.
[16] Zitzler-Kunkel A, Lenze MR, Schnier T, Meerholz K, Würthner F. Comparative studies on optical, redox, and photovoltaic properties of a series of D–A–D and analogous D–A chromophores. Adv Funct Mater 2014;24:4645–53.
[17] Aytun T, Barreda L, Ruiz-Carretero A, Lehrman JA, Stupp SI. Improving solar cell efficiency through hydrogen bonding: a method for tuning active layer morphology. Chem Mater 2015;27:1201–9.
[18] Li Z, He G, Wan X, Liu Y, Zhou J, Long G, et al. Solution processable rhodanine-based small molecule organic photovoltaic cells with a power conversion efficiency of 6.1%. Adv Energy Mater 2012;2:74–7.
[19] Long G, Wan X, Kan B, Liu Y, He G, Li Z, et al. Investigation of quinquethiophene derivatives with different end groups for high open circuit voltage solar cells. Adv Energy Mater 2013;3:639–46.
[20] Winzenberg KN, Kemppinen P, Fanchini G, Bown M, Collis GE, Forsyth CM, et al. Dibenzo[b,def]chrysene derivatives: solution-processable small molecules that deliver high power-conversion efficiencies in bulk heterojunction solar cells. Chem Mater 2009;21:5701–3.
[21] Lloyd MT, Mayer AC, Subramanian S, Mourey DA, Herman DJ, Bapat AV, et al. Efficient solution-processed photovoltaic cells based on an anthradithiophene/fullerene blend. J Am Chem Soc 2007;129:9144–9.
[22] Wong WWH, Singh TB, Vak D, Pisula W, Yan C, Feng X, et al. Solution processable fluorenyl hexa-peri-hexabenzocoronenes in organic field-effect transistors and solar cells. Adv Funct Mater 2010;20:927–38.
[23] Tamayo AB, Walker B, Nguyen T-Q. A low band gap, solution processable oligothiophene with a diketopyrrolopyrrole core for use in organic solar cells. J Phys Chem C 2008;112:11545–51.
[24] Kumar CHP, Ganesh K, Suresh T, Sharma A, Bhanuprakash K, Sharma GD, et al. Influence of thermal and solvent annealing on the morphology and photovoltaic performance of solution processed, D-A-D type small molecule-based bulk heterojunction solar cells. RSC Adv 2015;5:93579–90.
[25] Dittmer JJ, Lazzaroni R, Leclère P, Moretti P, Granström M, Petritsch K, et al. Crystal network formation in organic solar cells. Sol Energy Mater Sol Cells 2000;61:53–61.
[26] Mayukh M, Macech MR, Placencia D, Cao Y, Armstrong NR, McGrath DV. Solution processed titanyl phthalocyanines as donors in solar cells: photoresponse to 1000 nm. ACS Appl Mater Interfaces 2015;7:23912–9.
[27] Elsawy W, Lee C-L, Cho S, Oh S-H, Moon S-H, Elbarbary A, et al. Isoindigo-based small molecules for high-performance solution-processed organic photovoltaic devices: the electron donating effect of the donor group on photo-physical properties and device performance. Phys Chem Chem Phys 2013;15:15193–203.
[28] Stalder R, Mei J, Graham KR, Estrada LA, Reynolds JR. Isoindigo, a versatile electron-deficient unit for high-performance organic electronics. Chem Mater 2014;26:664–78.
[29] Lee OP, Yiu AT, Beaujuge PM, Woo CH, Holcombe TW, Millstone JE, et al. Adv Mater 2011;23:5359–63.
[30] Kim K-H, Yu H, Kang H, Kang DJ, Cho C-H, Cho H-H, et al. Influence of intermolecular interactions of electron donating small molecules on their

molecular packing and performance in organic electronic devices. J Mater Chem A 2013;1:14538–47.
[31] Ahn Y, Jang DE, Cha Y-B, Kim M, Ahn K-H, Kim YC. Bull Korean Chem Soc 2013;34:107–11.
[32] Marszalek M, Nagane S, Ichake A, Humphry-Baker R, Paul V, Zakeeruddin SM, et al. Tuning spectral properties of phenothiazine based donor-[small pi]-acceptor dyes for efficient dye-sensitized solar cells. J Mater Chem 2012;22:889–94.
[33] Chang YJ, Chou P-T, Lin Y-Z, Watanabe M, Yang C-J, Chin T-M, et al. Organic dyes containing oligo-phenothiazine for dye-sensitized solar cells. J Mater Chem 2012;22(40):21704–12.
[34] Luo J-S, Wan Z-Q, Jia C-Y. Recent advances in phenothiazine-based dyes for dye-sensitized solar cells. Chin Chem Lett 2016;27:1304–18.
[35] Li K-C, Hsu Y-C, Lin J-TS, Yang C-C, Wei K-H, Lin H-C. Novel narrow-band-gap conjugated copolymers containing phenothiazine-arylcyanovinyl units for organic photovoltaic cell applications. J Polym Sci Part A Polym Chem 2008;46:4285–304.
[36] Maglione C, Carella A, Centore R, Chávez P, Lévêque P, Fall S, et al. Novel low bandgap phenothiazine functionalized DPP derivatives prepared by direct heteroarylation: application in bulk heterojunction organic solar cells. Dyes Pigments 2017;141:169–78.
[37] Stille JK. The palladium-catalyzed cross-coupling reactions of organotin reagents with organic electrophiles [new synthetic methods (58)]. Angewandte Chemie Int Ed Engl 1986;25:508–24.
[38] Knoevenagel E. Berichte Dtsch Chem Ges 1898;31:2596–619.
[39] Shao Y, Molnar LF, Jung Y, Kussmann J, Ochsenfeld C, Brown ST, et al. Advances in methods and algorithms in a modern quantum chemistry program package. Phys Chem Chem Phys 2006;8(27):3172–91.
[40] Juang T-Y, Hsu Y-C, Jiang B-H, Chen C-P. Highly efficient inverted organic photovoltaics containing aliphatic hyperbranched polymers as cathode modified layers. Macromolecules 2016;49(20):7837–43.
[41] Chang C-C, Jiang B-H, Li Y-C, Chen C-P, Cheng C-H. Indacenodithiophene-based conjugated polymers incorporating alkylthiophene side chains: improvement of organic solar cell performance. Dyes Pigments 2017;142:139–46.
[42] Jiang B-H, Peng Y-J, Chen C-P. Simple structured polyetheramines, jeffamines, as efficient cathode interfacial layers for organic photovoltaics providing power conversion efficiencies up to 9.1%. J Mater Chem A 2017;5:10424–9.